



Surface oxygen vacancies prompted the formation of hydrated hydroxyl groups on ZnO_x in enhancing interfacial catalytic ozonation

Yizhen Cheng^{a,b}, Jing Kang^a, Pengwei Yan^{a,*}, Jimin Shen^a, Zhonglin Chen^{a,*}, Xinwei Zhu^a, Qiang Tan^a, Linlu Shen^a, Shuyu Wang^a, Shaobin Wang^b

^a State Key Laboratory of Urban Water Resources and Environment, School of Environment, Harbin Institute of Technology, Harbin 150090, China

^b School of Chemical Engineering, The University of Adelaide, Adelaide, SA 5005, Australia

ARTICLE INFO

Keywords:

Oxygen vacancies
Surface hydroxyl groups
Catalytic ozonation
ZnO_x
Density functional theory

ABSTRACT

Herein, a highly dispersed catalyst (ZnO_x-500) was synthesized for heterogeneous catalytic ozonation (HCO), which had a simple ZnO crystal phase but riched in oxygen vacancies (OVs). The O₃/ZnO_x-500 system exhibited both superior catalytic activity and stability after several cycles, providing a promising strategy for atrazine (ATZ) removal. The strong inhibition of phosphoric acid validated the dominant role of the hydroxyl group (–OH) from water molecule (H₂O) dissociation on the zinc site near OVs. Density functional theory calculation further revealed that OVs on (100) and (101) planes could make more zinc sites exposed and facilitate the formation of hydrated –OH, which was easier to approach O₃ for its decomposition to generate hydroxyl radical (•OH). This work revealed the intrinsic relationship between OVs and hydrated –OH in an aqueous solution, providing new insight into the solid-liquid interface mechanism of HCO.

1. Introduction

Heterogeneous catalytic ozonation (HCO) has been receiving increasing attention in pollutant abatement [1,2]. The HCO is benefited from the strong oxidability of ozone (O₃) ($E^0 = 2.07$ V), which can not only attack contaminants directly but also be decomposed to non-selective hydroxyl radicals (•OH) ($E^0 = 1.8$ – 2.7 V) for high-efficient mineralization [3,4]. Thus, HCO has excellent applicability in improving O₃ utilization rate and enhancing decontamination effectiveness [5–7]. For this reason, a variety of heterogeneous catalysts have emerged. According to previous reports, many metal-based catalysts, such as FeOOH [8], Fe₃O₄ [9], α-Fe₂O₃ [10], MgO [11], MnO₂ [12], CeO₂ [13], and LaCoO₃ [14], could drive O₃ decomposition and produce reactive oxygen species (ROS). The catalytic capacity of those catalysts usually depends on their intrinsic active components, while an in-depth understanding of the interface reaction is still controversial.

Previous works have suggested that surface hydroxyl groups (–OH) were of great significance for catalytic ozonation by metal-oxide catalysts, which are favorable for O₃ decomposition to produce ROS through an ion exchange bridge [15]. However, a variety of hydroxyl groups are present in metal oxides, necessitating a more precise distinction of their respective activities in HCO. Zhang et al. proposed that the uncharged

surface –OH on FeOOH was the active site to generate •OH [16], and also revealed that different surface –OH groups of oxo-hydroxides could take part in catalytic ozonation with varying activities [8]. Zhao et al. reported that the –OH from the dissociation of adsorbed water (H₂O) on the metal oxide surface was the active site, and that both strong electrophilic hydrogen and nucleophilic oxygen atoms on chemisorbed –OH could react with dipole molecules of O₃ [17]. Recent studies have proved that oxygen vacancies (OVs) expose more metal sites and the hydrated –OH from H₂O dissociation plays a leading role in catalytic ozonation [18–20]. Hence, the catalytic capacity of metal oxides depends on the catalysts riched in OVs and endowed with hydrophilic properties, which could be targeted to induce the formation of hydrated –OH from H₂O.

Zinc oxide (ZnO) is a hexagonal wurtzite, which has been widely used as a catalyst, photodetector and sensor attributed to its semiconductor properties [21,22]. A few studies have explored the HCO mechanism in respect of the surface –OH of ZnO in water [23]. However, the OVs in ZnO may lead to unexpected electron redistribution, which has always been overlooked in previous work [24]. Moreover, there are differences in the adsorption and dissociation of H₂O on different exposed crystal facets within metal oxides. Additionally, O₃ adsorption on metal oxides is the first step to induce interfacial

* Corresponding authors.

E-mail addresses: pengweiyan_hit@163.com (P. Yan), zhonglinchen@hit.edu.cn (Z. Chen).

<https://doi.org/10.1016/j.apcatb.2023.123325>

Received 31 May 2023; Received in revised form 15 September 2023; Accepted 21 September 2023

Available online 24 September 2023

0926-3373/© 2023 Elsevier B.V. All rights reserved.

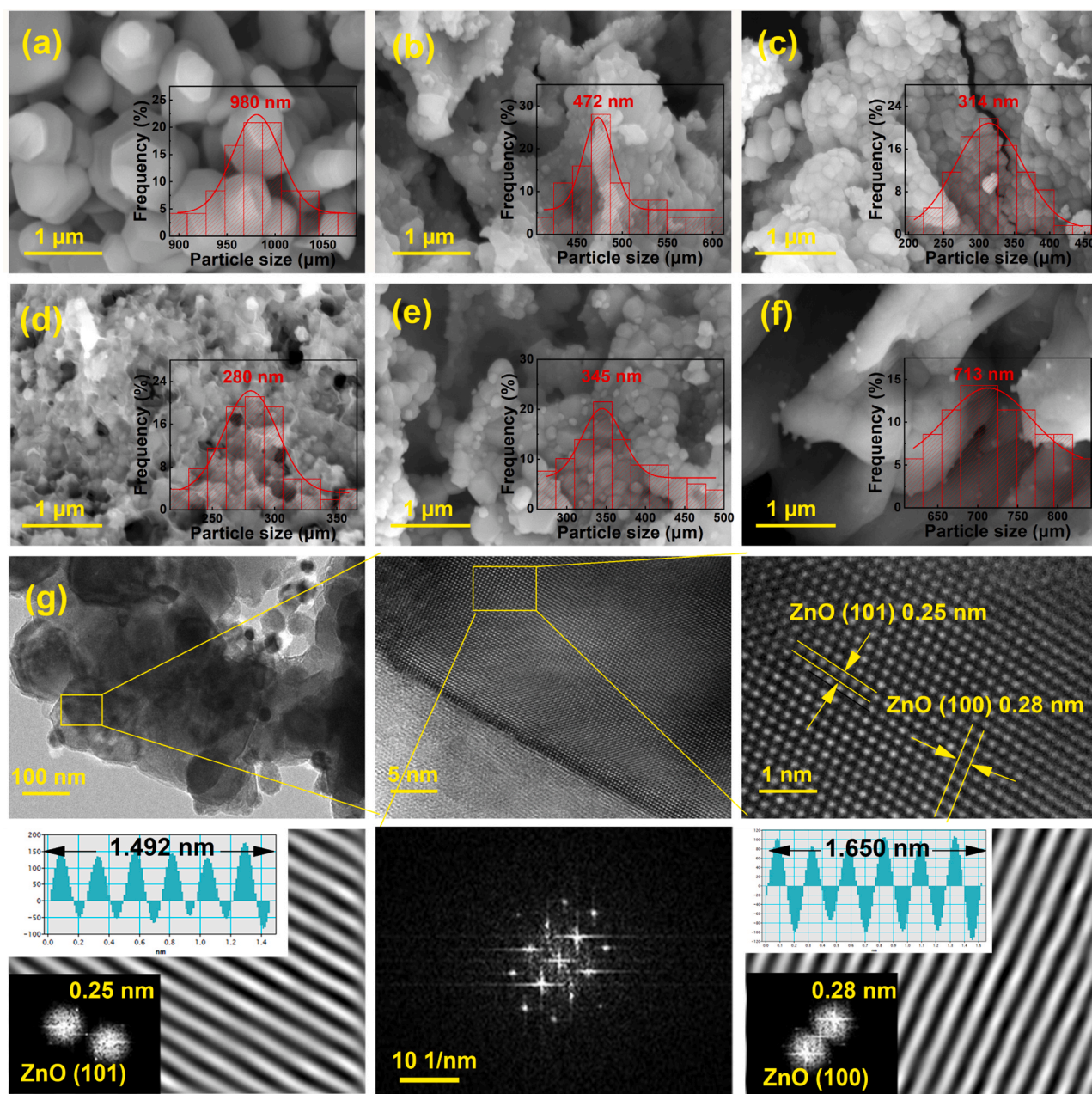


Fig. 1. Surface morphology analysis of the catalysts. SEM images and particle size distributions (inset) of (a) pristine ZnO, (b) ZnO_x-400, (c) ZnO_x-500, (d) ZnO_x-600, (e) ZnO_x-700, and (f) ZnO_x-800. (g) HRTEM images of ZnO_x-500.

reactions, which has not been given enough attention [25]. Thus, it is highly imperative to advance the understanding of the decomposition behavior of O₃ on metal oxides and adsorption kinetics.

In this study, a typical catalyst (ZnO_x) rich in OV was synthesized and employed for catalytic ozonation. Atrazine (ATZ), a typical herbicide in water and refractory to O₃ ($k_{O_3/ATZ} = 6.0 M^{-1} s^{-1}$), was identified as a model compound. A novel relationship between OV and hydrated -OH was uncovered by tracking the decomposition behavior of O₃ on the catalyst by ATR-FTIR, in-situ Raman spectroscopy and density functional theory (DFT) calculation. This work brings a new understanding of the intrinsic structural characteristics of ZnO_x and the in-depth mechanism of catalytic ozonation.

2. Materials and methods

2.1. Materials

Urea (99 %), atrazine (ATZ, 99 %), *p*-chlorobenzoic acid (*p*-CBA, >99 %), *tert*-butanol (TBA, 99 %), dimethyl sulfoxide (DMSO, 99.9 %), furfuryl alcohol (FFA, 98 %), methanol (MeOH, 99 %), chloroform (99 %), *N,N*-diethyl-*p*-phenylenediamine (DPD, 98 %), horseradish peroxidase (POD, RZ>2.5) and 4-chloro-7-nitrobenzo-2-oxa-1,3-diazole (NBD-Cl, 98 %) were supplied by Aladdin Biochemical Co., Ltd (China). 5,5-Dimethyl-1-pyrroline N-oxide (DMPO, >97 %) and 2,2,6,6-tetramethyl-4-piperidinol (TEMP, >99 %) were purchased from Merck Co., Ltd (Germany). Zinc nitrate hexahydrate (Zn(NO₃)₂·6 H₂O, 99 %) and humic acid (HA, 98 %) were obtained from Macklin Biochemical Co., Ltd (China). All experiments were conducted with deionized (DI) water.

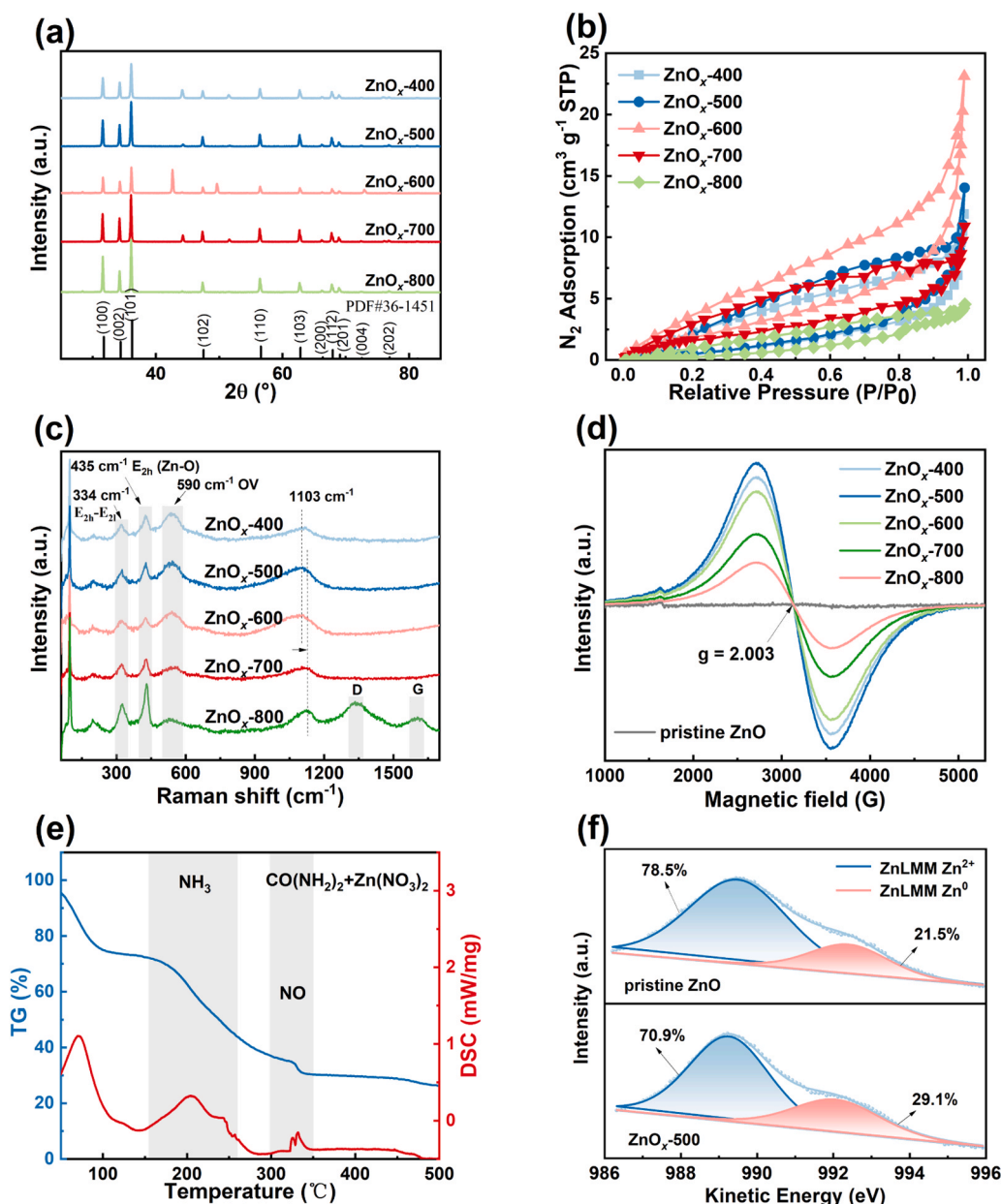


Fig. 2. Characterizations of the catalysts. (a) XRD spectra. (b) Nitrogen adsorption-desorption isotherms. (c) Raman spectra. (d) Solid-ESR spectra. (e) TG and DSC curves of a mixture of urea and zinc nitrate. (f) ZnLMM Auger spectra of pristine ZnO and ZnO_x-500.

2.2. Preparation of ZnO_x

ZnO_x was synthesized via a facile one-pot method. Briefly, 3 g zinc nitrate hexahydrate was first blended into 50 % ethanol. Subsequently, urea was added to the mixture with a mole ratio of 1:4, co-stirred for 4 h, and then dried at 60 °C. The obtained precursor was calcined at a certain temperature (400–800 °C) for 2 h. The whole pyrolysis process was performed in a tube furnace with a nitrogen atmosphere. After the sample was cooled down, it was washed 3 times with DI water, followed by drying in an oven for 24 h. The prepared sample was denoted as ZnO_x-*T*, where *T* represented the calcination temperature (ZnO_x-500 with the best activity was used for the study). For comparison, a sample without urea was also fabricated at 500 °C and labeled as pristine ZnO, and the samples without zinc nitrate hexahydrate were named as C-*T* (*T* = 400–800 °C).

2.3. Characterizations

The morphology analysis of catalysts was performed by a scanning electron microscope (SEM, ZEISS, UK). The structural texture of catalysts was analyzed by a high-resolution transmission electron microscope (HRTEM, JEOL, Japan). An X-ray diffractometer (XRD, Bruker, Germany) was used to observe crystalline structure. The chemical states of elements were identified by X-ray photoelectron spectroscopy (XPS, Thermo Fisher, USA). The chemical vibrations were captured by a Raman spectrometer (HORIBA, Japan). Electron spin resonance (ESR, Bruker, Germany) was used to detect the presence of uncoupled electrons in the catalyst and ROS generation during ozonation (Text S1). The acid sites of catalysts were calculated by a Fourier transform-infrared spectroscopy instrument (FTIR, Bruker, Germany) after the adsorption of pyridine. The pyrolysis process of the precursor was monitored by a simultaneous thermal analyzer-mass spectrometer (NETZSCH, Germany). The contact angle was tested by the Tensiometer (DSA100,

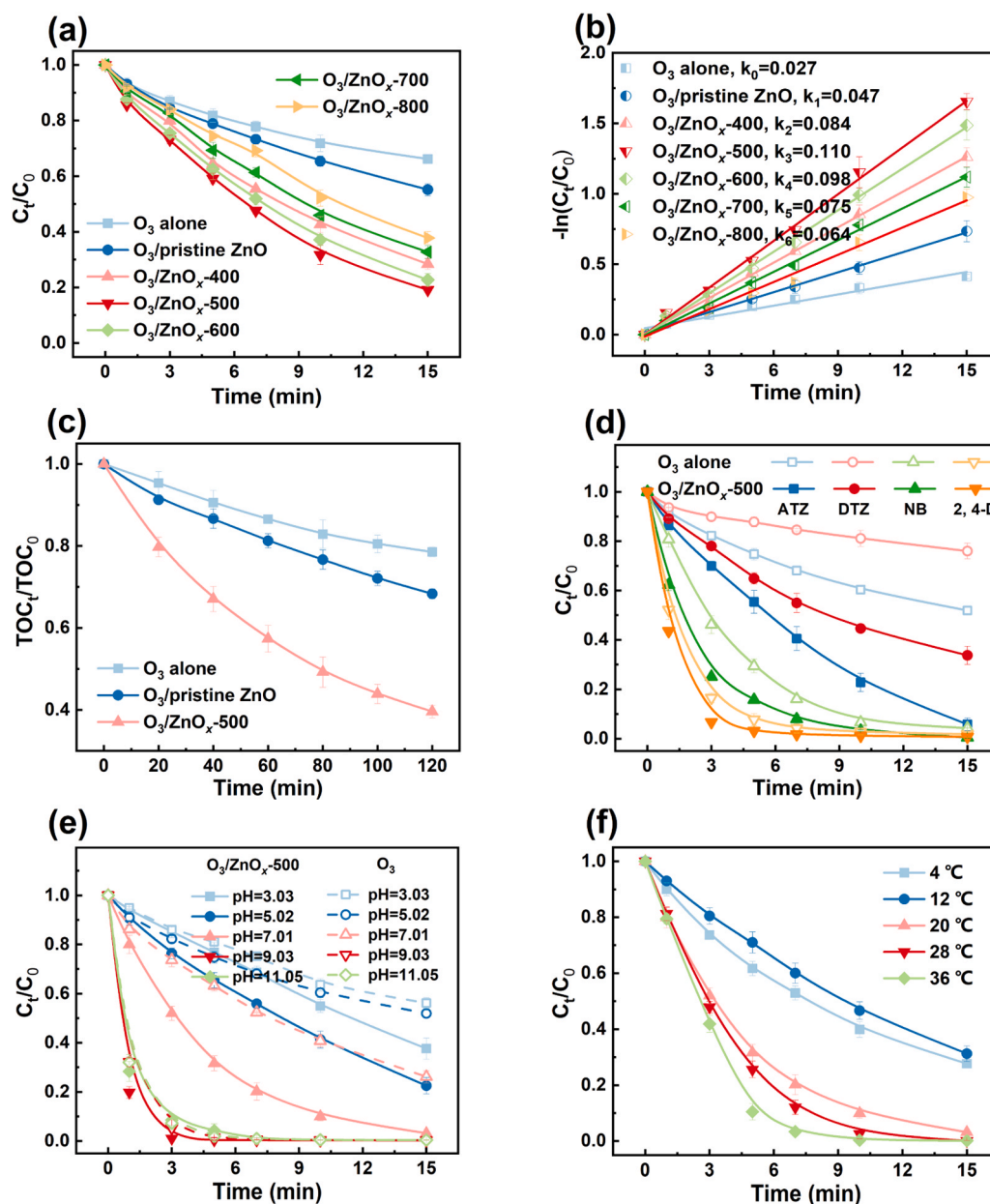


Fig. 3. Catalytic activity of the catalysts. (a) Removal rate and (b) kinetics of ATZ by pristine ZnO and ZnO_x in different ozonation systems. (c) Removal of TOC under different ozonation systems. (d) Removal of different contaminants by ZnO_x-500 in catalytic ozonation. Effects of (e) solution pH and (f) temperature on ATZ degradation performance by ZnO_x-500 in catalytic ozonation. Conditions: [ATZ]₀ = 5 μM, [O₃] = 3.62 mg min⁻¹ (for a) and 5.87 mg min⁻¹ (for b-f), [catalyst] = 40 mg L⁻¹ (except c) and 100 mg L⁻¹ (for c), T = 20 °C and pH = 5.86 (except e).

Germany).

2.4. Catalytic procedures

The typical HCO process was taken place in a 1 L semi-batch glass flask, and an ATZ stock solution was added at the very beginning to form a uniformly dispersed 5 μM ATZ solution. Subsequently, the catalyst (40 mg L⁻¹) was put in the solution, and then O₃ was continuously bubbled into (0.1 L min⁻¹) during the whole reaction through an ozone generator (ANSEROS, Germany) equipped with oxygen (99.99 %). The reactor was designed with a porous ceramic diffuser at the bottom and a magnetic stir (1000 rpm) to achieve a uniform reaction. At different time intervals, 2 mL suspensions were obtained, quenched rapidly by Na₂SO₃ (0.01 M), and then filtered for further UPLC analysis. The anions (NO₃⁻, SO₄²⁻, Cl⁻, HCO₃⁻, HPO₄²⁻) were added to the solution before

introducing the catalyst, and the pH was regulated by 0.1 M NaOH or H₂SO₄. All data are the mean of three replicates.

2.5. Analysis methods

ATZ and *p*-CBA were identified by ultrahigh-performance liquid chromatography (UPLC) at 221 and 240 nm, respectively. Parameters of the mobile phase were shown in Text S2. The intermediates were investigated by a UPLC-QTOF/MS spectrometer (Agilent 6545, USA). Ion chromatography (ICS-OES, iCAP 7400, Thermo, Germany) was employed to evaluate the leached zinc ions. The concentrations of dissolved O₃ and gaseous O₃ were measured by indigo [26] and iodometric [27] methods, respectively. The amount of O₃ adsorbed on the surface was quantified based on our previous work [28], and detailed descriptions were shown in Text S3. The time-dependent amount of

hydrogen peroxide (H_2O_2) was estimated according to the DPD/POD method [29]. TBA and NBD-Cl were used as the chemical probes to investigate the concentrations of $\cdot\text{OH}$ and superoxide radical ($\text{O}_2^{\cdot-}$), respectively (Text S4) [30–32]. The attenuated total reflection-FTIR (ATR-FTIR) analysis was performed in heavy water (D_2O) to observe hydrated $-\text{OD}$ formed by D_2O dissociation on the catalyst surface (Text S5). In-situ Raman signal was measured on an infiltrated catalyst permeated uniformly by ozone solution (10 mg L^{-1}). The procedures of electrochemical analysis were described in Text S6. The determination of the density of surface hydrated $-\text{OH}$ was displayed in Text S7.

2.6. Theoretical calculations

The optimization of the $2 \times 2 \times 2$ super-cell structure, the calculation of adsorption energy (E_{ads}) and the density of states (DOS) of the optimized structures were based on the CASTEP package [33]. The generalized gradient approximation (GGA) with the PBE functional equation was conducted and the Grimme method was used for the DFT-D correction.

3. Results and discussion

3.1. Characterizations

Fig. 1a shows that pristine ZnO has an agglomerated hexagonal wurtzite structure [34]. When zinc nitrate hexahydrate and urea were co-pyrolyzed at different calcination temperatures (400–800 °C) in a ratio of 1:4, the morphology of the samples changed remarkably. Specifically, the dispersion of ZnO_x particles increased and some irregular pore structures appeared as the pyrolysis temperature rose from 400 to 600 °C (Fig. 1b–d). However, it would further be consolidated at a temperature of 700–800 °C (Figs. 1e and 1f), which may be uncondusive to the exposure of the active site, making its catalytic activity inferior. Fig. S1 displays the EDS distribution of ZnO_x -500, where the Zn/O atomic ratio was 4:3, suggesting the lack of oxygen atoms and formation of OV_s in the structure, as well as consistent with the results of XPS survey spectra (Fig. S2). Especially, its high deconvolution of O 1s displayed that lattice oxygen (O_{lat}) was the dominant component, while the OV_s (O_{vac}) decreased with the increase of temperature, reaching its peak in ZnO_x -500 (Fig. S3). Notably, two legible lattice stripes (0.25 and 0.28 nm) were identified within ZnO_x -500 according to HRTEM images (Fig. 1g), which were indexed to the (100) and (101) planes of ZnO crystals, respectively [35]. These findings could also be confirmed by XRD patterns in Fig. 2a. The diffraction peaks were undoubtedly attributed to the hexagonal wurtzite structure (PDF#36-1451), similar to pristine ZnO (Fig. S4) [36] and confirming ZnO nanoparticles.

Nitrogen adsorption-desorption isotherms of ZnO_x were depicted in Fig. 2b. The specific surface area (SSA) of ZnO_x gradually increased to $4.82 \text{ m}^2 \text{ g}^{-1}$ (Table S1) at 600 °C and then decreased at higher pyrolysis temperature, which was in accordance with SEM analyses. Fig. 2c shows Raman spectra with three characteristic signals at 334, 435 and 590 cm^{-1} , which can be indexed to the second-order multiphonon mode of $\text{E}_{2\text{h}}-\text{E}_{2\text{l}}$, vibration mode of $\text{E}_{2\text{h}}$ (Zn–O) and OV_s, respectively [37]. It should be noticed that the intensity of OV_s increased slightly from 400 to 500 °C, but it decreased quickly from 500 to 800 °C. Moreover, the peak at 1103 cm^{-1} blue-shifted as the pyrolysis temperature increased, and the peaks of disordered carbon (D) and graphitic carbon (G) also appeared at 800 °C. It was probable that the higher temperature reduced the interatomic distance, making the aggregation of ZnO_x nanoparticles.

The solid ESR confirmed that the signal at $g = 2.003$ attributed to OV_s in ZnO nanoparticles reached the highest level in ZnO_x -500 and decreased substantially when pyrolysis temperature further increased (Fig. 2d and Fig. S5), in accord with the Raman results (Fig. 2c). To further reveal the formation of the abundant OV_s in ZnO_x -500, we checked the TG and DSC curves of a mixture of urea and zinc nitrate. As shown in Fig. 2e, the combustion process of the mixture has three main

weight loss stages, coordinated with the DSC endothermic signals at 80, 240 and 325 °C. It can be recognized that the first loss at nearly 80 °C was due to the evaporation of free water, while the losses at 240 and 325 °C were ascribed to the release of NH_3 and NO by the decomposition of urea and zinc nitrate during the pyrolysis process, respectively [38, 39]. These two reducing gases (NH_3 and NO) could be further illustrated by the TG and DSC of urea and zinc nitrate alone (Fig. S6) and their online MS curves of all pre-samples (Fig. S7), which endowed the possibility of Zn^{2+} being reduced to Zn^0 during the calcination process.

To validate the speculation, we conducted ZnLMM Auger electron spectroscopy to determine the reduced Zn^0 on pristine ZnO and ZnO_x -500 [40]. It can be inferred from Fig. 2f that Zn^{2+} can be reduced to Zn^0 (21.5 %) in pristine ZnO by NO, while NH_3 produced by urea may further promote a larger amount of Zn^0 (29.1 %) in ZnO_x -500. Therefore, to maintain the valance balance in the structure, oxygen atoms would be lacking and the OV_s were formed, which may render free electrons and catalytic activity of the catalysts [41].

3.2. Catalytic performance and stability evaluation

3.2.1. Catalytic performance of ZnO_x

The catalytic performance of ZnO_x at different pyrolysis temperatures was displayed in Fig. 3a. Compared to the low ATZ removal efficiencies in O_3 alone (33.8 %) and O_3 /pristine ZnO (44.8 %) systems, O_3 / ZnO_x -500 has shown the best catalytic efficiency for ATZ degradation (80.9 %), which may attribute to ZnO_x -500 nanoparticles with a less particle size (314 nm) and a large number of OV_s. The highest reaction rate constant (0.110 min^{-1}) also indicated the rapid degradation ability of the O_3 / ZnO_x -500 system (Fig. 3b). It should be noticed that all single carbon materials without ZnO have limited activity (Fig. S8). Therefore, ZnO_x -600 with an apparent coating of inert C_3N_4 (Figs. 1d and 2a) hindered its catalytic ozonation capability albeit it has the lowest particle size (280 nm). Additionally, all the catalysts exhibited a poor adsorption capacity of ATZ (< 5 %) (Fig. S9). We compared a group of ZnO_x -T-Air prepared under air conditions. Similar catalytic activities could also be observed (Fig. S10), while a bit weak catalytic activities may be related to their poor dispersion and large ZnO particle size (Fig. S11), as well as the lower contents of OV_s (Fig. S12). Thus, highly dispersed ZnO nanoparticles were active components in catalytic ozonation, and a small amount of carbon substrate evidenced by TG (Fig. S13) can promote the better dispersion of ZnO and the formation of OV_s.

Subsequently, ZnO_x -500 was used to further probe the influences of ZnO_x -500 dosage, O_3 dosage and initial ATZ concentration (Fig. S14). The results showed that more catalysts and O_3 dosage would bring more active sites and oxidants, driving more ATZ degradation. However, the increment of initial ATZ concentration may compete for limited ROS, leading to a decrease in degradation rates. As shown in Fig. 3c, there was nearly 60.4 % of TOC removal in O_3 / ZnO_x -500 system, which was much larger than that of O_3 alone (21.5 %) and O_3 /pristine ZnO systems (31.7 %). It should be notable that the O_3 / ZnO_x -500 system could still maintain highly catalytic performance for different contaminants (Fig. 3d). These findings suggested that a highly active catalytic system (O_3 / ZnO_x -500) has been successfully established.

3.2.2. Influences of pH and temperature on catalytic activity

Solution pH is of paramount importance for the behavior of O_3 decomposition, and surface electrification of pollutants and catalysts, which would further affect the degradation efficiency of contaminants during catalytic ozonation. Fig. 3e illustrates that the removal rate of ATZ was facilitated significantly at pH from 3.03 to 9.03, but it reduced slightly at pH 11.05. This phenomenon was similar to the previous studies [42,43]. Considering the pH_{pzc} of ZnO_x -500 at 7.58 (Fig. S15), its surface would be protonated at $\text{pH} < \text{pH}_{\text{pzc}}$. Therefore, it may reduce the nucleophilicity of hydrated $-\text{OH}$ in an acidic solution, which was not conducive to the interaction with O_3 . Moreover, it may cause the

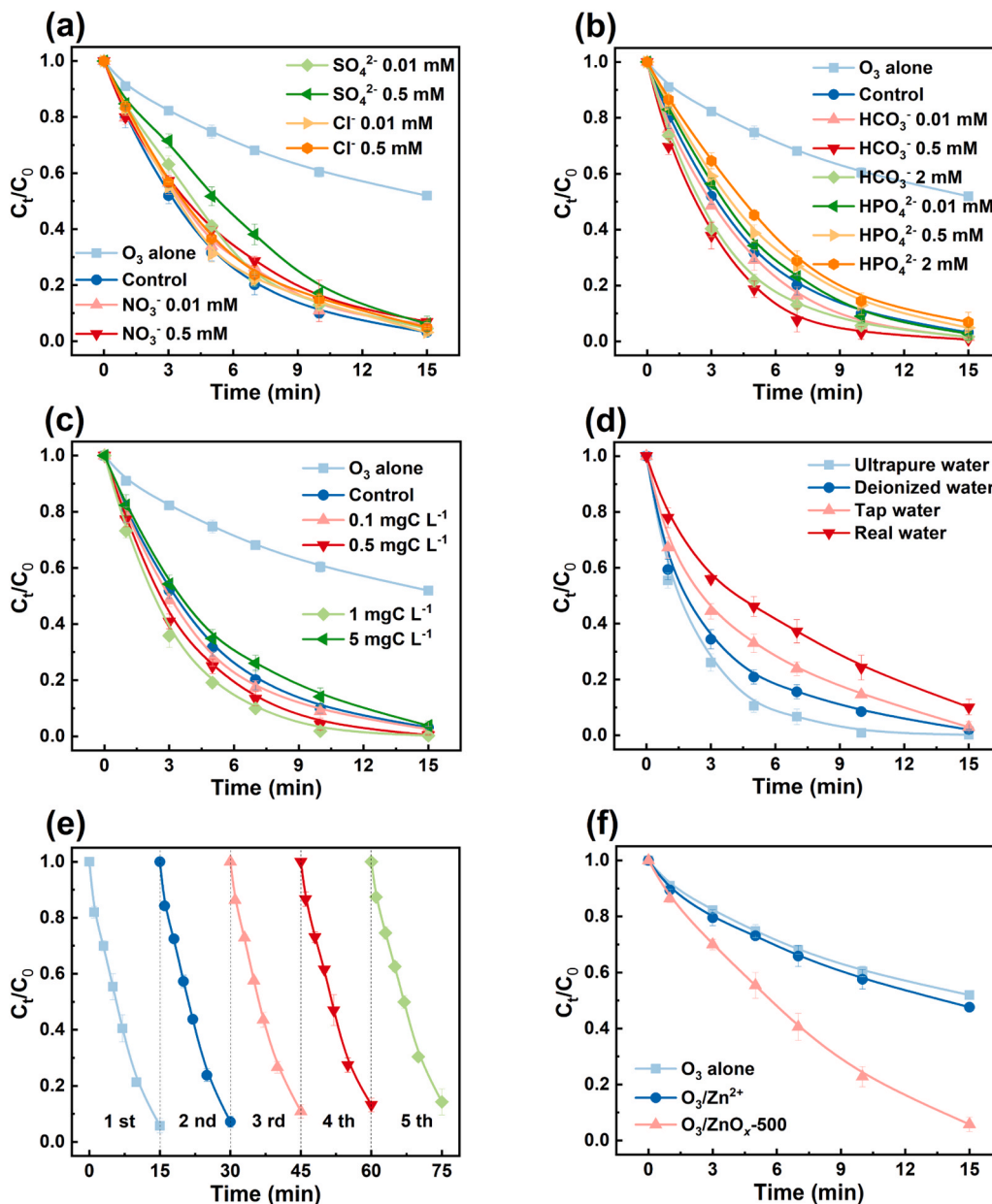
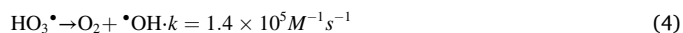
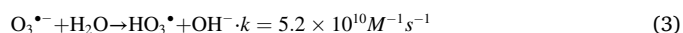
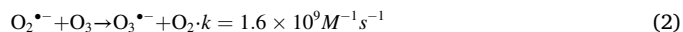
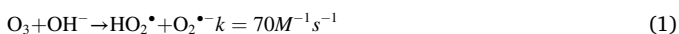


Fig. 4. Effects of (a, b) inorganic anions, (c) humic acid, and (d) different water backgrounds on ATZ degradation in O_3/ZnO_x-500 system. (e) Reusability tests of ZnO_x-500 . (f) Removal of ATZ by released zinc ions in homogeneous catalytic ozonation. Conditions: $[ATZ]_0 = 5 \mu M$, $[O_3] = 5.87 \text{ mg min}^{-1}$, $[catalyst] = 40 \text{ mg L}^{-1}$ (except d) and 100 mg L^{-1} (for d), $T = 20^\circ \text{C}$ and $pH = 7.01$ (for a-d) and 5.86 (for e, f).

leaching of Zn^{2+} at a low solution pH (3.03), resulting in the poor catalytic activity of ZnO_x-500 [44]. As the pH was raised from 7.58 to 9.03, the surface of ZnO_x-500 underwent deprotonation, resulting in enhanced electrostatic repulsion interaction with ATZ ($pK_a = 1.7$). It may lead to the weakening of the heterogeneous catalytic process. However, during this pH range, the presence of OH^- in water strengthened the homogeneous catalytic reaction of O_3 (Eqs. (1)–(4)), resulting in the effective coupling of both homogeneous and heterogeneous catalytic ozonation, peaking at $pH = 9.03$. Furthermore, ZnO_x-500 was mostly deprotonated at $pH = 11.05$, at which a homogeneous process was only involved. Meanwhile, the electrophilic hydrogen of hydrated $-OH$ would enter into the reaction solution at a higher pH, resulting in inferior catalytic activity to that at $pH = 9.03$ [17].



The solution temperature could affect the decontamination efficiency by changing ozone solubility and the reactant activity of ozone and organic pollutants. As shown in Fig. 3f, low temperature brings low mass-transfer efficiency, but the catalytic activity at 4°C (72.3 %) was higher than that at 12°C (68.7 %), which may be attributed to the high solubility of ozone. As the temperature increased, the degradation efficiency was further promoted due to the higher reactant molecular activity.

3.2.3. Catalytic stability and degradation pathway

The stabilities of catalytic capacity and structure of ZnO_x-500 were

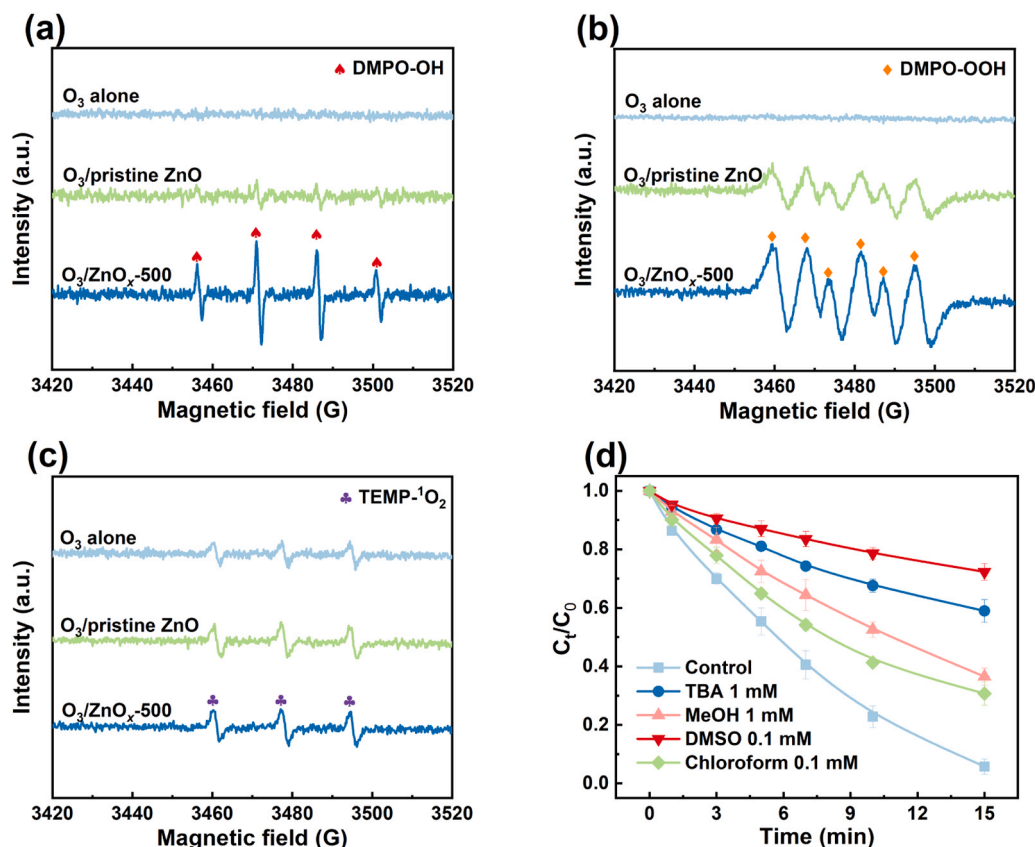


Fig. 5. Investigation of ROS. ESR identification of (a) hydroxyl radicals, (b) superoxide radicals, and (c) singlet oxygen. (d) Effects of radical scavengers on ATZ removal. Conditions: [ATZ]₀ = 5 μ M (for d), [O₃] = 5.87 mg min⁻¹, [catalyst] = 40 mg L⁻¹, [DMPO] = 0.084 M (for a, b), [TEMP] = 0.084 M (for c), T = 20 °C and pH = 5.86.

also investigated. The presence of inorganic anions (NO₃⁻, SO₄²⁻, Cl⁻, HCO₃⁻, HPO₄²⁻) in the solution usually interferes the catalytic system. Fig. 4a shows that NO₃⁻ and Cl⁻ had little interference on ATZ removal, while 0.5 mM SO₄²⁻ had resulted in a certain delay in the degradation rate, which may be attributed to the steric hindrance, suppressing the collision rate of O₃ on the surface. Similarly, the same phenomenon was observed in the inhibition of HPO₄²⁻ (Fig. 4b), acting as a stronger Lewis base compared to H₂O to significantly reduce ATZ degradation by replacing the hydrated -OH [45]. Regarding HCO₃⁻, its weak effect may be attributed to the interfacial reaction triggered by O₃ adsorbed on hydrated -OH, which was not readily disturbed by anions in the solution. A slightly positive effect of HCO₃⁻ at relatively lower levels was observed, similar to a previous work for bicarbonate on H₂O₂ (a typical active species in ozonation) [46]. Humic acid (HA) is a natural organic matter (NOM) in real water. Fig. 4c shows that a lower concentration of HA (0.1–1 mgC L⁻¹) could promote the degradation of ATZ, which may be attributed to the phenolic and ammonium of HA that could react with O₃ to produce [•]OH [47]. However, excessive HA would compete with ATZ to react with O₃ or quench [•]OH, and occupy the active sites on the catalyst surface [48,49]. Thus, it was necessary to investigate the performance of the O₃/ZnO_x-500 system under different water backgrounds.

Surprisingly, the ATZ removal rate in real water (RW) only decreased by 9.9 % compared with that in ultrapure water after 15 min of reaction (Fig. 4d). The significant reduction of dissolved organic matter (DOM) in RW further indicated the excellent catalytic stability of the O₃/ZnO_x-500 system in real water (Fig. S16). Fig. 4e demonstrates that ZnO_x-500 presented an 8.5 % reduction of ATZ degradation efficiency after five cycles, with a low level of Zn²⁺ leached percentage, which was less than 2 % (0.7 mg L⁻¹, below the limit of 3 mg L⁻¹ set by WHO) (Fig. S17). It suggests that ZnO_x-500 exhibited excellent stability in catalytic activity

and structure. Considering that the leached Zn²⁺ may also be a potential factor in promoting O₃ decomposition, 1.0 mg L⁻¹ Zn²⁺ was added to trigger HCO (Fig. 4f). However, the leached zinc ions only played a minor role in catalytic ozonation, confirming the high-efficient heterogeneous catalytic system of O₃/ZnO_x-500.

In this process, the degradation intermediates of ATZ were also identified and seven products were found (Table S2). The possible degradation pathways of ATZ included de-alkylation, alkylic-hydroxylation, dechlorination-hydroxylation and alkylic-oxidation. Fig. S18 shows that ATZ would be attacked by ROS to form P1 and P2 during de-alkylation, which were further transformed into P5 [50]. The formation of P3 was based on the alkylic-hydroxylation of ATZ, and it would be further converted to P6 and P7 through de-alkylation and dechlorination-hydroxylation, respectively. Moreover, the dechlorination process was also an essential way of ATZ degradation, which can be confirmed by the generation of P4 [51].

3.3. Recognition of ROS

In-situ ESR was conducted to recognize potential ROS generated in O₃/ZnO_x-500 system. Fig. 5a shows the strongest characteristic signal of DMPO-OH in O₃/ZnO_x-500 system among all the ozonation systems, indicating that ZnO_x-500 could significantly induce [•]OH production by O₃ decomposition. When methanol was used as the reaction solution to eliminate [•]OH interference, higher intensity DMPO-OOH suggested that O₂^{•-} was also involved in O₃/ZnO_x-500 system (Fig. 5b). However, the signal of TEMP-¹O₂ was detected in all the systems with no significant difference in their intensity, suggesting an unvital role of ¹O₂ in ATZ degradation (Fig. 5c). Thus, quenching tests were further employed to distinguish the different roles of ROS in O₃/ZnO_x-500 system.

Fig. 5d reveals that only 27.7 %, 41.0 % and 63.5 % of ATZ were

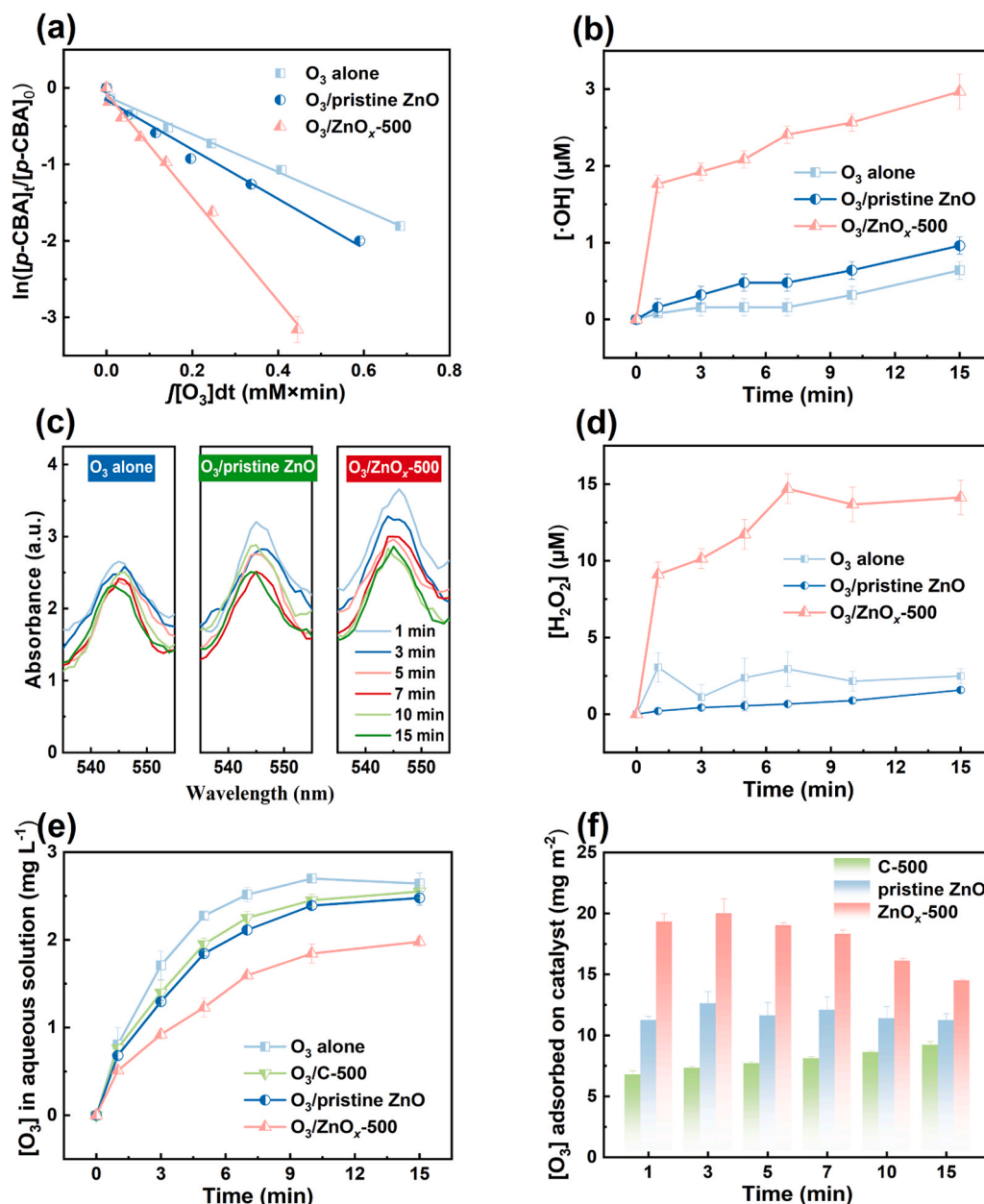


Fig. 6. ROS production and ozone utilization. (a) R_{ct} values in different systems by p -CBA as probe compound. Time-dependent variation of (b) hydroxyl radicals, (c) superoxide radicals and (d) hydrogen peroxide formed in different ozonation systems. The concentration of O_3 (e) in aqueous solution and (f) adsorbed on catalysts. Conditions: $[O_3] = 5.87\ mg\ min^{-1}$, $[catalyst] = 40\ mg\ L^{-1}$, $T = 20\ ^{\circ}C$ and $pH = 5.86$, $[p\text{-CBA}]_0 = 0.1\ mM$ (for a), $[TBA]_0 = 1\ mM$ (for b), $[NBD\text{-}Cl]_0 = 0.1\ mM$ (for c), $[ATZ]_0 = 5\ \mu M$ (for d-f).

degraded in 15 min when DMSO, TBA and MeOH were applied as the inhibitors of $^{\bullet}OH$, respectively. It is implied that $^{\bullet}OH$ played the dominant role in ATZ degradation and the different affinity for ZnO_x-500 may be responsible for the different inhibition effects between the three inhibitors. Specifically, DMSO can effectively quench $^{\bullet}OH$ both on catalysts and in solution with a fast reaction rate ($k_{OH/DMSO} = 5.4 \times 10^9\ M^{-1}s^{-1}$), while TBA ($k_{OH/TBA} = 6.0 \times 10^8\ M^{-1}s^{-1}$) and MeOH ($k_{OH/MeOH} = 9.7 \times 10^8\ M^{-1}s^{-1}$) are difficult to capture $^{\bullet}OH$ on catalysts (Fig. S19) [3,52]. Chloroform is a typical inhibitor for $O_2^{\bullet-}$ ($k_{O_2^{\bullet-}/chloroform} = 2.3 \times 10^8\ M^{-1}s^{-1}$) because of its low reaction rates with $^{\bullet}OH$ ($k_{OH/chloroform} = 5.4 \times 10^7\ M^{-1}s^{-1}$) and O_3 ($k_{O_3/chloroform} \leq 0.1\ M^{-1}s^{-1}$) [53]. A little inhibitory effect of 0.1 mM chloroform and low reaction rate ($k_{O_2^{\bullet-}/ATZ} = 4.1 \times 10^5\ M^{-1}s^{-1}$) indicated that $O_2^{\bullet-}$ was also involved but did not play a dominant role. These findings demonstrated that

ZnO_x-500 could induce $^{\bullet}OH$ and $O_2^{\bullet-}$ production from O_3 decomposition, but $^{\bullet}OH$ took a key part in ATZ removal.

The different contribution of ROS was further quantified by the chemical probe method. R_{ct} was identified as a ratio of $^{\bullet}OH$ to O_3 exposure, which was determined by a probe compound, p -CBA ($k_{OH/p\text{-CBA}} = 5.2 \times 10^9\ M^{-1}s^{-1}$) [54]. As shown in Fig. 6a, a higher R_{ct} (1.2×10^9) was obtained in the O_3 /ZnO_x-500 system, indicating that more O_3 can be decomposed into $^{\bullet}OH$ by ZnO_x-500 for ATZ degradation. Moreover, TBA was applied as a typical probe to qualify produced $^{\bullet}OH$ (0.5 mol formaldehyde produced by combining 1 mol $^{\bullet}OH$) [32]. Fig. 6b reveals the time-dependent variation process of $^{\bullet}OH$ during catalytic ozonation. The accumulative $^{\bullet}OH$ in the O_3 /ZnO_x-500 system reached 2.97 μM after 15 min, which was much higher than in the other systems. However, when using an NBD-Cl probe to detect formed $O_2^{\bullet-}$ [31], the fluorescence signals could hardly change in different ozonation systems

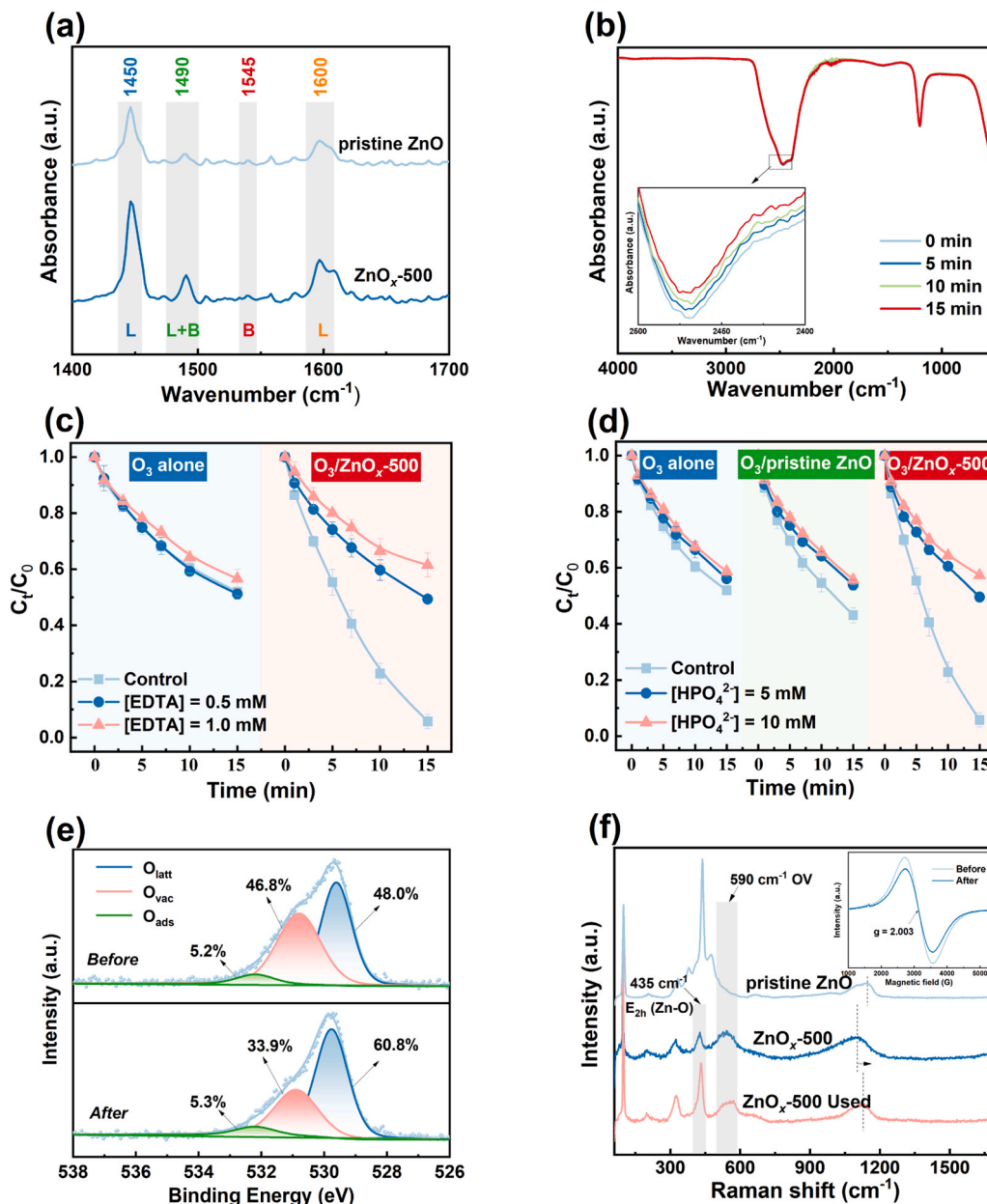


Fig. 7. Verification of catalytic active sites. (a) Pyridine-FTIR spectra of pristine ZnO and ZnO_x-500. (b) *In-situ* ATR-FTIR spectra of O₃/ZnO_x-500 in D₂O. Effects of (c) EDTA and (d) phosphate on ATZ removal in different ozonation systems. (e) XPS O 1s spectra of ZnO_x-500 before and after catalytic ozonation. (f) Raman spectra of pristine ZnO and ZnO_x-500 before and after catalytic ozonation. Conditions: [ATZ]₀ = 5 μM, [O₃] = 5.87 mg min⁻¹, [catalyst] = 40 mg L⁻¹, T = 20 °C and pH = 5.86.

(Fig. 6c). It further suggested that $\cdot\text{OH}$ has a major contribution to ATZ degradation rather than $\text{O}_2^{\cdot-}$, which was in good accordance with the quenching tests.

H₂O₂ is a typical byproduct produced during ozonation through Criegee-type reactions and free radical chain-terminating reactions [55]. It is the only stable intermediate generated during ozonation, whose change could reflect the trend of O₃ decomposition. Fig. 6d displays that the amount of H₂O₂ was substantially accumulated to 14.13 μM within 15 min reaction in the O₃/ZnO_x-500 system, which may benefit from the contribution of radical chain reactions (Eqs. (5)–(7)). It suggested that ZnO_x-500 could enhance O₃ decomposition and ROS production.



To verify the transformation behavior of O₃ in the catalytic ozonation, we further detected the amounts of O₃ in solution and on catalysts. From Fig. 6e, ~1.98 mg L⁻¹ dissolved O₃ was found in O₃/ZnO_x-500 system, lower than that in O₃ alone (2.64 mg L⁻¹) and O₃/pristine ZnO systems (2.48 mg L⁻¹). It is validated that dissolved O₃ can be efficiently utilized by ZnO_x-500, whose behavior was further investigated in Fig. 6f. The amount of O₃ on the surface of C-500 and pristine ZnO remained at 9.2 and 11.3 mg m⁻² within 15 min reaction without further decomposition, while the amount of O₃ on the surface of ZnO_x-500 gradually decreased with the increased reaction time. Combined with the lower concentration of dissolved O₃ in the O₃/ZnO_x-500 system, it is elucidated that O₃ was efficiently utilized by the active sites of ZnO_x-500 and then decomposed into ROS rapidly.

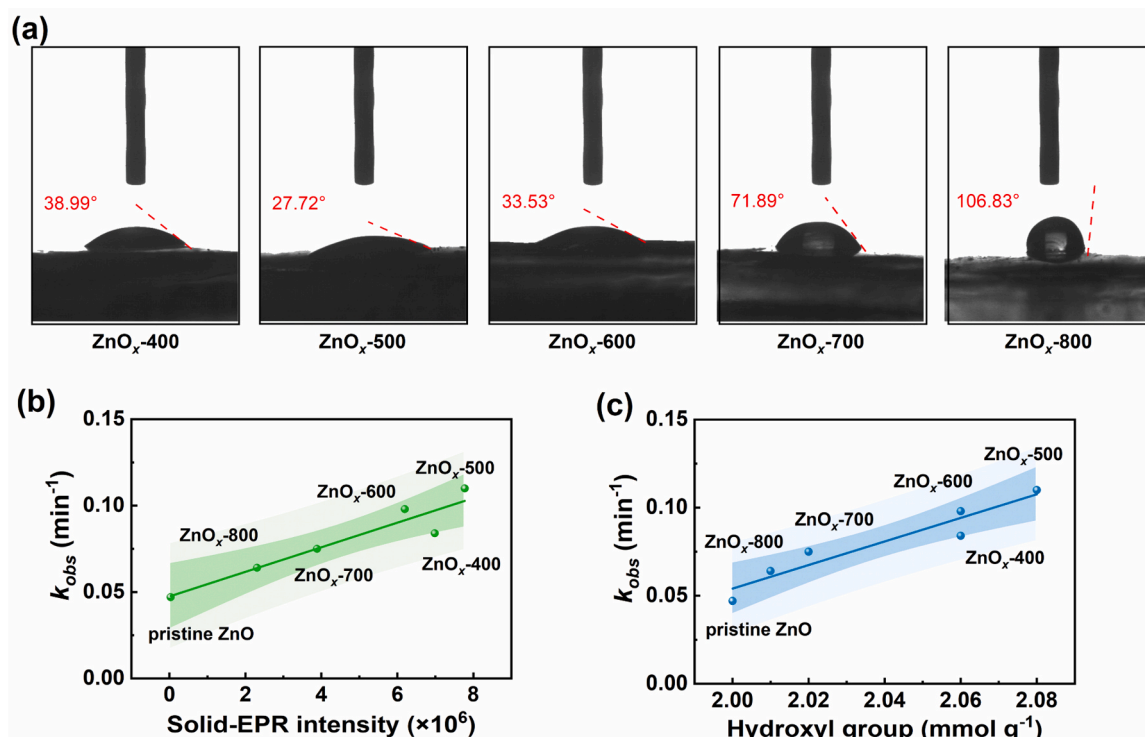


Fig. 8. (a) Contact angles of ZnO_x-T. The linear relationships between k_{obs} and (b) OVs and (c) hydrated -OH.

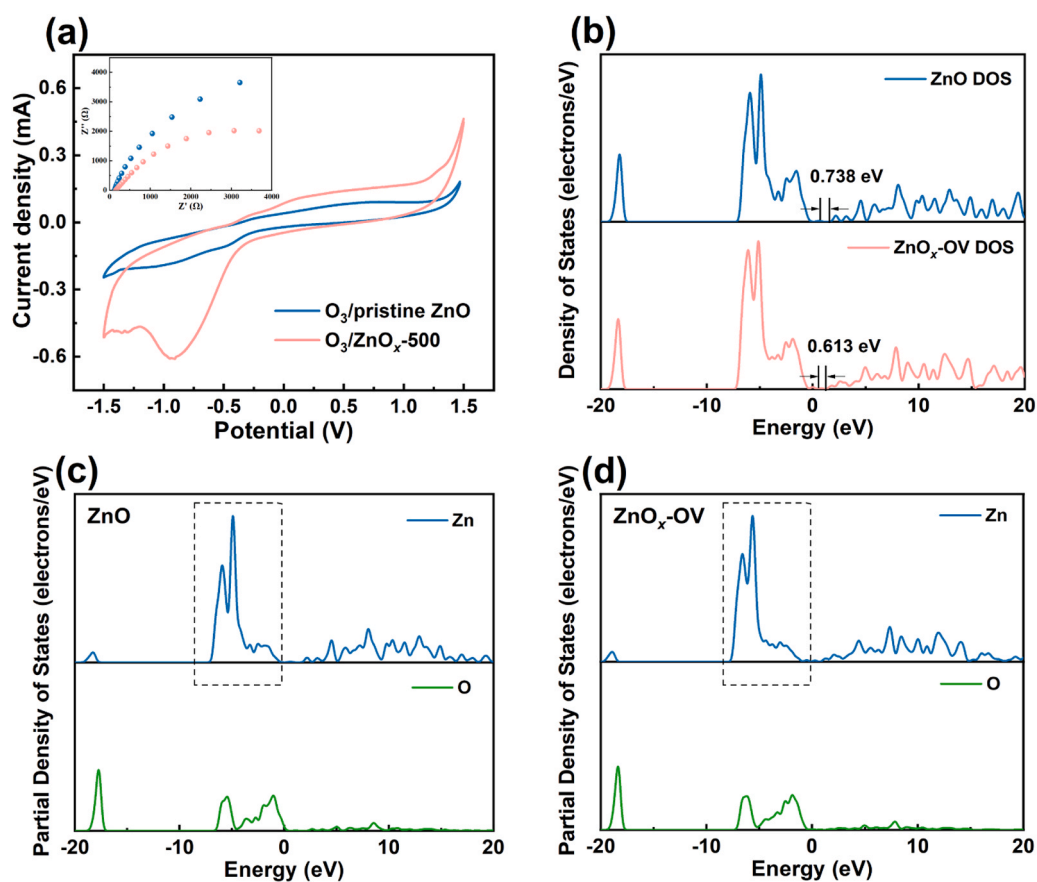


Fig. 9. Electrochemical experiments and theoretical calculations. (a) CV curves and EIS Nyquist plots (inset) of catalysts. (b) Density of states (DOS) of pristine ZnO and ZnO_x with an oxygen vacancy. Partial density of states (PDOS) of (c) pristine ZnO and (d) ZnO_x-OV.

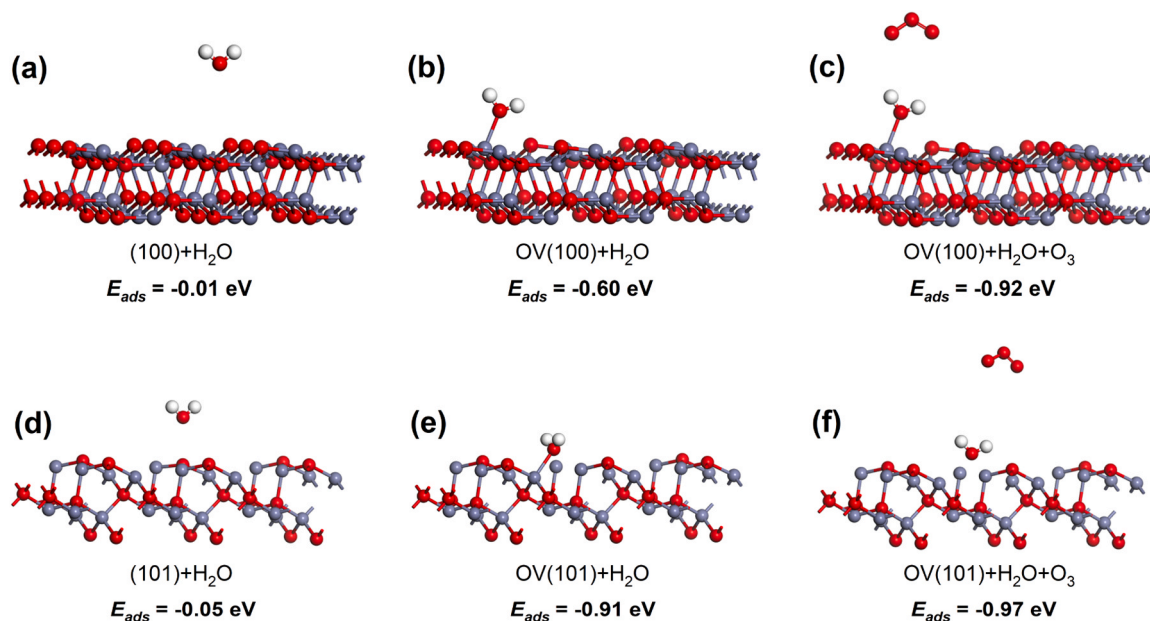


Fig. 10. The adsorption energies of H_2O or O_3 molecules onto the (100) and (101) planes of (a, d) pristine ZnO and (b, c, e, f) $\text{ZnO}_x\text{-OV}$.

3.4. Identification of potential active sites

Lewis acid sites (LAS) are usually considered to be potential active sites of metal-based catalysts, which can be characterized by pyridine FTIR [56]. Typical IR bands at 1450 and 1600 cm^{-1} were indexed to the adsorption of pyridine on strong LAS (Fig. 7a), which are responsible for the decomposition of O_3 [57]. The signal centered at 1490 cm^{-1} was assigned to Lewis and Brønsted acid sites, but the peak at 1545 cm^{-1} was attributed to strong Brønsted acid sites, which could only enhance the aggregation and adsorption of O_3 on catalysts [58]. Other trivial peaks may be attributed to unadsorbed pyridine. Notably, a higher amount of total LAS occurred on $\text{ZnO}_x\text{-500}$ ($19.37\text{ }\mu\text{mol g}^{-1}$) than on pristine ZnO ($9.97\text{ }\mu\text{mol g}^{-1}$) calculated by the method [59]. It is indicated that the $\text{ZnO}_x\text{-500}$ could expose more zinc ions on its surface, which were conducive to the adsorption of O_3 or H_2O .

Compared with the finite dissolved O_3 in the solution, $\text{ZnO}_x\text{-500}$ was contacted by H_2O molecules during the whole reaction. The adsorption of H_2O on $\text{ZnO}_x\text{-500}$ could not be ignored. ATR-FTIR was performed to investigate the role of hydrated $-\text{OH}$ formed by H_2O adsorption on zinc ions. As shown in Fig. 7b, a D_2O solution was applied to distinguish the hydrated $-\text{OD}$ bonded with metal ions and the bulk $-\text{OH}$ in water. The stretching vibration of $-\text{OD}$ in metal (MeO-D) was located at 2470 cm^{-1} [60], which decreased in the $\text{O}_3/\text{ZnO}_x\text{-500}$ system during catalytic ozonation. The signal at 1200 cm^{-1} came from the vibration of hydrogen-bonded D_2O [61]. It revealed that metal ions might be the active center that could form hydrated $-\text{OH}$ by adsorbing and dissociating H_2O [62]. This conclusion can also be confirmed via the experiments on the complexation of surface metal ions by EDTA and the substitution of hydrated $-\text{OH}$ by HPO_4^{2-} .

Fig. 7c shows that the catalytic activity of $\text{ZnO}_x\text{-500}$ was significantly inhibited when EDTA at low concentrations was presented in the reaction solution. EDTA would be complexed with zinc ions, hindering the formation of hydrated $-\text{OH}$ [63]. Furthermore, HPO_4^{2-} is a stronger Lewis base than H_2O [45], resulting in a dramatical decrease in ATZ degradation by substituting the surface $-\text{OH}$ (Fig. 7d). The O_3 decomposition was inhibited when hydrated $-\text{OH}$ was substituted by HPO_4^{2-} (Fig. S20a), and this kind of $-\text{OH}$ proved more active than structural $-\text{OH}$ (Fig. S20b). Meanwhile, a decreased amount of O_3 on the catalyst could also be observed, reflected in lower $[\text{O}_3]$ in the solution after 12 h as the $[\text{HPO}_4^{2-}]$ increased (Fig. S21). Moreover, Fig. 8 elucidates the remarkable hydrophilicity of $\text{ZnO}_x\text{-500}$, with a measured contact angle

of 27.72° , surpassing that of other catalysts synthesized at higher temperatures. Additionally, robust correlations were established between k_{obs} and OVs as well as hydrated $-\text{OH}$. These discoveries confirm the role of OVs in facilitating the exposure of a greater number of metal ions, thereby amplifying the generation of hydrated $-\text{OH}$ species through the dissociation of adsorbed H_2O molecules.

The structural features of $\text{ZnO}_x\text{-500}$ before and after reactions were also investigated. Fig. 7e displays that the amount of lattice oxygen increased, but the number of OVs reduced from 46.8 % to 33.9 % after the reaction, which was in accord with the reduction of Zn^0 content (Fig. S22). The same phenomenon can also be observed in Raman and solid-EPR analyses before and after the reaction (Fig. 7f). It was hypothesized that OVs also contributed to the decomposition of O_3 by tweaking the local electronic structure [64]. Notably, a new characteristic peak appeared at 884 cm^{-1} in the in-situ Raman spectrum, corresponding to the adsorbed peroxide species ($^*\text{O}_2$) (Fig. S23), which consistently originated from the decomposition of O_3 at metal cation sites [65]. And the $^*\text{O}_2$ species was found to be associated with the generation of $\text{O}_2^{\cdot-}$ and $^1\text{O}_2$ [66–68]. However, the leading role of $^*\text{OH}$ for ATZ removal has been demonstrated, while $\text{O}_2^{\cdot-}$ and $^1\text{O}_2$ only contributed partly. Therefore, it further validated the importance of the surface dissociated $-\text{OH}$ near OVs for ATZ degradation, which was more effective than the direct reaction between O_3 and OVs.

3.5. DFT simulation and possible catalytic mechanism

Based on the larger active surface area and lower impedance of $\text{ZnO}_x\text{-500}$ than pristine ZnO (Fig. 9a), the DFT calculations were performed to unveil the decomposition behavior of O_3 on different active sites of $\text{ZnO}_x\text{-500}$ and the internal relationship between surface dissociated $-\text{OH}$ and OVs. Firstly, two models of a pristine ZnO crystal (ZnO) and defective ZnO_x with an OV ($\text{ZnO}_x\text{-OV}$) as $\text{ZnO}_x\text{-500}$ were established (Fig. S24). According to the density of states (DOS) in Fig. 9b, compared to pristine ZnO (0.738 eV), the energy band gap of $\text{ZnO}_x\text{-OV}$ is narrowed to 0.613 eV with an OV in the ZnO crystal. It is indicated that OVs may bring impurity energy levels in the band gap, which will be beneficial for electron transition [69]. It should be noted that its shorter bandwidth than the actual value may be caused by the GGA method overestimating the three-dimensional orbital energy of Zn and reducing the bandwidth, but the calculated results would not affect the electronic structure analysis [70]. Notably, the partial density of states (PDOS) of Zn

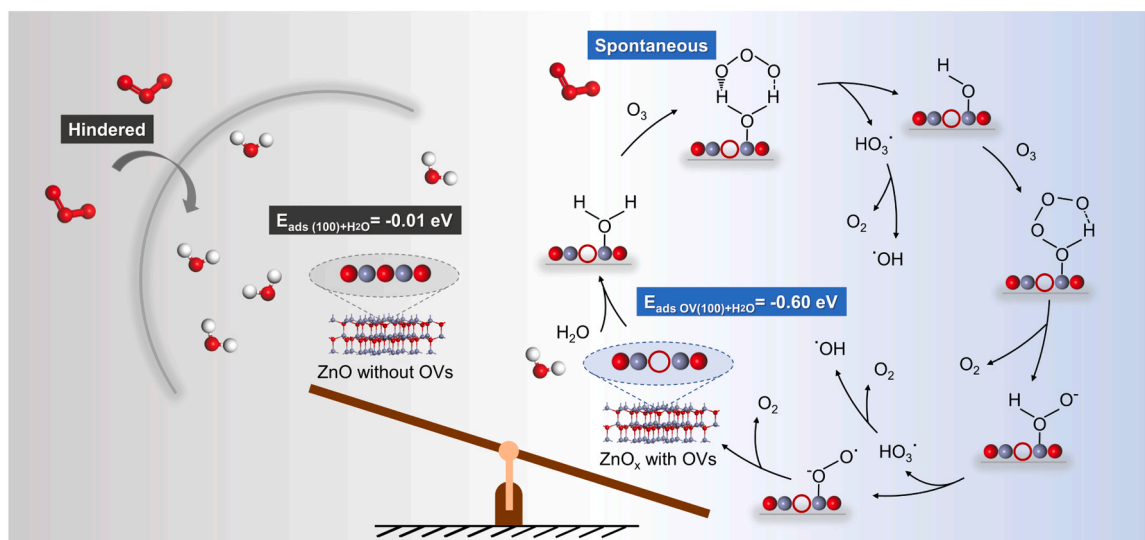


Fig. 11. Possible interface catalytic mechanisms.

increased in the presence of OVs (Fig. 9c and d), suggesting OVs could make more zinc ions exposed and increase the electronic contribution of Zn orbitals to total DOS.

For further verification, the adsorption energies (E_{ads}) of H₂O and O₃ molecules onto the (100) and (101) planes of pristine ZnO and ZnO_x-OV were also calculated. As shown in Fig. 10, the lower E_{ads} (−0.60 and −0.91 eV) of ZnO_x-OV indicated that the ZnO_x-OV was easier to approach H₂O molecule than pristine ZnO (−0.01 and −0.05 eV). Then, O₃ was easily adsorbed on hydrated −OH formed by zinc ions dissociating H₂O, according to their lowest E_{ads} (−0.92 and −0.97 eV). In this process, the polar (100) plane was more effective than the non-polar (101) plane.

Therefore, the main interface catalytic mechanisms were driven by hydrated −OH dissociated from H₂O (Fig. 11). Due to a large number of OVs, more zinc ions were exposed on the surface of ZnO_x-500 to facilitate the formation of surface −OH. It enabled the association of O₃ and lead to the generation of HO₃•, which would rapidly convert into •OH ($k = 1.4 \times 10^5 \text{ M}^{-1} \text{ s}^{-1}$).

4. Conclusions

A heterogeneous catalyst (ZnO_x-500) riched in OVs was synthesized through a one-step method and tested in catalytic ozonation. The O₃/ZnO_x-500 system achieved the best catalytic efficiency for ATZ degradation (80.9 %) than O₃ alone (33.8 %) and O₃/pristine ZnO (44.8 %) systems, attributed to its high dispersibility of ZnO and a large number of OVs. More importantly, a novel relationship between hydrated −OH and OVs was unraveled according to the strong inhibition of phosphoric acid and DFT calculation. It is recognized that OVs could make more zinc ions exposed and facilitate the formation of hydrated −OH by dissociating adsorbed H₂O, more favorable to O₃ approach than the original OVs. •OH produced by surface dissociated −OH was proved to take a dominant ATZ degradation. This work provided new insight into HCO in water purification.

CRediT authorship contribution statement

Yizhen Cheng: Conceptualization, Methodology, Investigation, Visualization, Validation, Data curation, Writing – original draft. **Jing Kang:** Formal analysis. **Pengwei Yan:** Conceptualization. **Jimin Shen:** Investigation during the revision stage. **Zhonglin Chen:** Resources, Project administration. **Xinwei Zhu:** Formal analysis. **Qiang Tan:** Validation. **Linlu Shen:** Validation. **Shuyu Wang:** Validation. **Shaobin**

Wang: Validation, Writing – review & editing.

Declaration of Competing Interest

The authors declare that they have no known competing financial interests or personal relationships that could have appeared to influence the work reported in this paper.

Data availability

Data will be made available on request.

Acknowledgements

The work was supported by the Heilongjiang Province Postdoctoral Fund (Grant No. LBH-Z22142) and the Open Project of State Key Laboratory of Urban Water Resource and Environment (Harbin Institute of Technology) (Grant No. QA202321).

Appendix A. Supporting information

Supplementary data associated with this article can be found in the online version at [doi:10.1016/j.apcatb.2023.123325](https://doi.org/10.1016/j.apcatb.2023.123325).

References

- [1] J. Wang, H. Chen, Catalytic ozonation for water and wastewater treatment: recent advances and perspective, *Sci. Total Environ.* 704 (2020), 135249.
- [2] A. Asghar, H.V. Lutze, J. Tuerk, T.C. Schmidt, Influence of water matrix on the degradation of organic micropollutants by ozone based processes: a review on oxidant scavenging mechanism, *J. Hazard. Mater.* 429 (2022), 128189.
- [3] Y. Wang, J. Xi, X. Duan, W. Lv, H. Cao, C. Chen, Z. Guo, Y. Xie, S. Wang, The duet of surface and radical-based carbocatalysis for oxidative destructions of aqueous contaminants over built-in nanotubes of graphite, *J. Hazard. Mater.* 384 (2020), 121486.
- [4] Y. Cheng, Z. Chen, S. Wang, X. Duan, Single atom catalysts for heterogeneous catalytic ozonation, *Curr. Opin. Chem. Eng.* 41 (2023), 100945.
- [5] Z. Song, J. Sun, W. Wang, Z. Wang, Y. Zhang, B. Xu, F. Qi, Stable synergistic decontamination and self-cleaning performance of powerful N-rGO catalytic ozonation membrane: Clustering effect of free electrons and role of interface properties, *Appl. Catal. B Environ.* 283 (2021), 119662.
- [6] B. Kasprzyk-Hordern, M. Ziślek, J. Nawrocki, Catalytic ozonation and methods of enhancing molecular ozone reactions in water treatment, *Appl. Catal. B Environ.* 46 (2003) 639–669.
- [7] F. Zhang, Q. Kong, H. Chen, X. Zhao, B. Yang, S. Preis, Zero valent boron activated ozonation for ultra-fast degradation of organic pollutants: atomic orbital matching, oxygen spillover and intra-electron transfer, *Chem. Eng. J.* 434 (2022), 134674.

- [8] T. Zhang, C. Li, J. Ma, H. Tian, Z. Qiang, Surface hydroxyl groups of synthetic α -FeOOH in promoting-OH generation from aqueous ozone: property and activity relationship, *Appl. Catal. B Environ.* 82 (2008) 131–137.
- [9] S. Zhu, B. Dong, Y. Yu, L. Bu, J. Deng, S. Zhou, Heterogeneous catalysis of ozone using ordered mesoporous Fe_3O_4 for degradation of atrazine, *Chem. Eng. J.* 328 (2017) 527–535.
- [10] X. Liang, L. Wang, T. Wen, H. Liu, J. Zhang, Z. Liu, C. Zhu, C. Long, Mesoporous poorly crystalline α - Fe_2O_3 with abundant oxygen vacancies and acid sites for ozone decomposition, *Sci. Total Environ.* 804 (2022), 150161.
- [11] H. Zhu, W. Ma, H. Han, Y. Han, W. Ma, Catalytic ozonation of quinoline using nano-MgO: efficacy, pathways, mechanisms and its application to real biologically pretreated coal gasification wastewater, *Chem. Eng. J.* 327 (2017) 91–99.
- [12] C. He, Y. Wang, Z. Li, Y. Huang, Y. Liao, D. Xia, S. Lee, Facet engineered α - MnO_2 for efficient catalytic ozonation of odor CH_3SH : oxygen vacancy-induced active centers and catalytic mechanism, *Environ. Sci. Technol.* 54 (2020) 12771–12783.
- [13] Q. Dai, J. Wang, J. Yu, J. Chen, J. Chen, Catalytic ozonation for the degradation of acetylsalicylic acid in aqueous solution by magnetic CeO_2 nanometer catalyst particles, *Appl. Catal. B Environ.* 144 (2014) 686–693.
- [14] Y. Zhang, Y. An, C. Liu, Y. Song, Z. Song, Y. Li, W. Meng, F. Qi, B. Xu, J.-P. Croue, D. Yuan, A. Ikhlaiq, Catalytic ozonation of emerging pollutant and reduction of toxic by-products in secondary effluent matrix and effluent organic matter reaction activity, *Water Res.* 166 (2019), 115026.
- [15] J. Nawrocki, M. Rigney, A. McCormick, P.W. Carr, Chemistry of zirconia and its use in chromatography, *J. Chromatogr. A* 657 (1993) 229–282.
- [16] T. Zhang, J. Ma, Catalytic ozonation of trace nitrobenzene in water with synthetic goethite, *J. Mol. Catal. A Chem.* 279 (2008) 82–89.
- [17] L. Zhao, Z. Sun, J. Ma, Novel relationship between hydroxyl radical initiation and surface group of ceramic honeycomb supported metals for the catalytic ozonation of nitrobenzene in aqueous solution, *Environ. Sci. Technol.* 43 (2009) 4157–4163.
- [18] P. Yan, J. Shen, Y. Zhou, L. Yuan, J. Kang, S. Wang, Z. Chen, Interface mechanism of catalytic ozonation in an α - $\text{FeO}_{0.9}\text{Mn}_{0.1}\text{OOH}$ aqueous suspension for the removal of iohexol, *Appl. Catal. B Environ.* 277 (2020), 119055.
- [19] Z. Zhang, H. Ai, M.-L. Fu, Y.-b Hu, J. Liu, Y. Ji, V. Vasudevan, B. Yuan, Oxygen vacancies enhancing performance of Mg-Co-Ce oxide composite for the selective catalytic ozonation of ammonia in water, *J. Hazard. Mater.* 436 (2022), 129000.
- [20] X. Chen, S. Zhan, D. Chen, C. He, S. Tian, Y. Xiong, Grey Fe- CeO_2 for boosting photocatalytic ozonation of refractory pollutants: roles of surface and bulk oxygen vacancies, *Appl. Catal. B Environ.* 286 (2021), 119928.
- [21] K.M. Lee, C.W. Lai, K.S. Ngai, J.C. Juan, Recent developments of zinc oxide based photocatalyst in water treatment technology: a review, *Water Res.* 88 (2016) 428–448.
- [22] J. Theerthagiri, S. Salla, R.A. Senthil, P. Nithyadarseni, A. Madankumar, P. Arunachalam, T. Maiyalagan, H.-S. Kim, A review on ZnO nanostructured materials: energy, environmental and biological applications, *Nanotechnology* 30 (2019), 392001.
- [23] X. Yuan, S. Duan, G. Wu, L. Sun, G. Cao, D. Li, H. Xu, Q. Li, D. Xia, Enhanced catalytic ozonation performance of highly stabilized mesoporous ZnO doped g- C_3N_4 composite for efficient water decontamination, *Appl. Catal. A Gen.* 551 (2018) 129–138.
- [24] G. Wen, S.-J. Wang, J. Ma, T.-L. Huang, Z.-Q. Liu, L. Zhao, J.-F. Su, Enhanced ozonation degradation of di-n-butyl phthalate by zero-valent zinc in aqueous solution: performance and mechanism, *J. Hazard. Mater.* 265 (2014) 69–78.
- [25] Z.-Q. Liu, J. Tu, Q. Wang, Y.-H. Cui, L. Zhang, X. Wu, B. Zhang, J. Ma, Catalytic ozonation of diethyl phthalate in aqueous solution using graphite supported zinc oxide, *Sep. Purif. Technol.* 200 (2018) 51–58.
- [26] H. Bader, J. Hoigné, Determination of ozone in water by the indigo method, *Water Res.* 15 (1981) 449–456.
- [27] D.L. Flamm, Analysis of ozone at low concentrations with boric acid buffered KI, *Environ. Sci. Technol.* 11 (1977) 978–983.
- [28] P. Yan, J. Shen, L. Yuan, J. Kang, B. Wang, S. Zhao, Z. Chen, Catalytic ozonation by Si-doped α - Fe_2O_3 for the removal of nitrobenzene in aqueous solution, *Sep. Purif. Technol.* 228 (2019), 115766.
- [29] H. Bader, V. Sturzenegger, J. Hoigné, Photometric method for the determination of low concentrations of hydrogen peroxide by the peroxidase catalyzed oxidation of N,N-diethyl-p-phenylenediamine (DPD), *Water Res.* 22 (1988) 1109–1115.
- [30] T. NASH, The colorimetric estimation of formaldehyde by means of the Hantzsch reaction, *Biochem. J.* 55 (1953) 416–421.
- [31] A. Ikhlaiq, D.R. Brown, B. Kasprzyk-Hordern, Mechanisms of catalytic ozonation: an investigation into superoxide ion radical and hydrogen peroxide formation during catalytic ozonation on alumina and zeolites in water, *Appl. Catal. B Environ.* 129 (2013) 437–449.
- [32] R. Flyunt, A. Leitzke, G. Mark, E. Mvula, E. Reisz, R. Schick, C. von Sonntag, Determination of OH^\cdot , $\text{O}_2^{\cdot-}$, and hydroperoxide yields in ozone reactions in aqueous solution, *J. Phys. Chem. B* 107 (2003) 7242–7253.
- [33] M.D. Segall, P.J.D. Lindan, M.J. Probert, C.J. Pickard, P.J. Hasnip, S.J. Clark, M. C. Payne, First-principles simulation: ideas, illustrations and the CASTEP code, *J. Phys. Condens. Matter* 14 (2002) 2717–2744.
- [34] C. Wichasilp, A. Phuruangrat, S. Thongtem, Influence of pH on the synthesis ZnO nanorods and photocatalytic hydrogen production from glycerol solution, *J. Indian Chem. Soc.* 99 (2022), 100472.
- [35] L. Sun, Q. Shao, Y. Zhang, H. Jiang, S. Ge, S. Lou, J. Lin, J. Zhang, S. Wu, M. Dong, Z. Guo, N self-doped ZnO derived from microwave hydrothermal synthesized zeolitic imidazolate framework-8 toward enhanced photocatalytic degradation of methylene blue, *J. Colloid Interface Sci.* 565 (2020) 142–155.
- [36] Y. Cheng, B. Wang, J. Shen, P. Yan, J. Kang, W. Wang, L. Bi, X. Zhu, Y. Li, S. Wang, L. Shen, Z. Chen, Preparation of novel N-doped biochar and its high adsorption capacity for atrazine based on π - π electron donor-acceptor interaction, *J. Hazard. Mater.* 432 (2022), 128757.
- [37] Y. Tang, H. Zhou, K. Zhang, J. Ding, T. Fan, D. Zhang, Visible-light-active ZnO via oxygen vacancy manipulation for efficient formaldehyde photodegradation, *Chem. Eng. J.* 262 (2015) 260–267.
- [38] K. Zhang, K. Zhang, Y. Cao, W.-p. Pan, Co-combustion characteristics and blending optimization of tobacco stem and high-sulfur bituminous coal based on thermogravimetric and mass spectrometry analyses, *Bioresour. Technol.* 131 (2013) 325–332.
- [39] W. Yang, L. Jia, P. Wu, H. Zhai, J. He, C. Liu, W. Jiang, Effect of thermal program on structure-activity relationship of g- C_3N_4 prepared by urea pyrolysis and its application for controllable production of g- C_3N_4 , *J. Solid State Chem.* 304 (2021), 122545.
- [40] S. Feliu, V. Barranco, XPS study of the surface chemistry of conventional hot-dip galvanised pure Zn, galvanneal and Zn-Al alloy coatings on steel, *Acta Mater.* 51 (2003) 5413–5424.
- [41] C. Zhang, M. Xu, Z. Yang, M. Zhu, J. Gao, Y.-F. Han, Uncovering the electronic effects of zinc on the structure of Fe_3C_2 -ZnO catalysts for CO_2 hydrogenation to linear α -olefins, *Appl. Catal. B Environ.* (2021), 120287.
- [42] P. Yan, Z. Chen, S. Wang, Y. Zhou, L. Li, L. Yuan, J. Shen, Q. Jin, X. Zhang, J. Kang, Catalytic ozonation of iohexol with α - $\text{FeO}_{0.9}\text{Mn}_{0.1}\text{OOH}$ in water: efficiency, degradation mechanism and toxicity evaluation, *J. Hazard. Mater.* 402 (2021), 123574.
- [43] Y. Cheng, B. Wang, P. Yan, J. Shen, J. Kang, S. Zhao, X. Zhu, L. Shen, S. Wang, Y. Shen, Z. Chen, In-situ formation of surface reactive oxygen species on defective sites over N-doped biochar in catalytic ozonation, *Chem. Eng. J.* 454 (2023), 140232.
- [44] L. Xing, Y. Xie, H. Cao, D. Minakata, Y. Zhang, J.C. Crittenden, Activated carbon-enhanced ozonation of oxalate attributed to HO-oxidation in bulk solution and surface oxidation: effects of the type and number of basic sites, *Chem. Eng. J.* 245 (2014) 71–79.
- [45] M. Sui, L. Sheng, K. Lu, F. Tian, FeOOH catalytic ozonation of oxalic acid and the effect of phosphate binding on its catalytic activity, *Appl. Catal. B Environ.* 96 (2010) 94–100.
- [46] L. Zhao, Z. Sun, J. Ma, H. Liu, Influencing mechanism of bicarbonate on the catalytic ozonation of nitrobenzene in aqueous solution by ceramic honeycomb supported manganese, *J. Mol. Catal. A Chem.* 322 (2010) 26–32.
- [47] Y. Yang, J. Jiang, X. Lu, J. Ma, Y. Liu, Production of sulfate radical and hydroxyl radical by reaction of ozone with peroxymonosulfate: a novel advanced oxidation process, *Environ. Sci. Technol.* 49 (2015) 7330–7339.
- [48] Y.-H. Guan, J. Ma, Y.-M. Ren, Y.-L. Liu, J.-Y. Xiao, L.-Q. Lin, C. Zhang, Efficient degradation of atrazine by magnetic porous copper ferrite catalyzed peroxymonosulfate oxidation via the formation of hydroxyl and sulfate radicals, *Water Res.* 47 (2013) 5431–5438.
- [49] Y. Cheng, J. Yang, J. Shen, P. Yan, S. Liu, J. Kang, L. Bi, B. Wang, S. Zhao, Z. Chen, Preparation of P-doped biochar and its high-efficient removal of sulfamethoxazole from water: adsorption mechanism, fixed-bed column and DFT study, *Chem. Eng. J.* 468 (2023), 143748.
- [50] Y. Huang, C. Han, Y. Liu, M.N. Nadagouda, L. Machala, K.E. O'Shea, V.K. Sharma, D.D. Dionysiou, Degradation of atrazine by $\text{ZnxCu}_{1-x}\text{Fe}_2\text{O}_4$ nanomaterial-catalyzed sulfate under UV-vis light irradiation: green strategy to generate $\text{SO}_4^{\cdot-}$, *Appl. Catal. B Environ.*, 221 (2018) 380–392.
- [51] X. Wang, Y. Liu, Z. Huang, L. Wang, Y. Wang, Y. Li, J. Li, J. Qi, J. Ma, Rapid oxidation of iodide and hypiodous acid with ferrate and no formation of iodoform and monoiodoacetic acid in the ferrate/ I^-/HA system, *Water Res.* 144 (2018) 592–602.
- [52] Y. Guo, J. Long, J. Huang, G. Yu, Y. Wang, Can the commonly used quenching method really evaluate the role of reactive oxygen species in pollutant abatement during catalytic ozonation? *Water Res.* (2022), 118275.
- [53] Y. Guo, Y. Zhang, G. Yu, Y. Wang, Revisiting the role of reactive oxygen species for pollutant abatement during catalytic ozonation: the probe approach versus the scavenger approach, *Appl. Catal. B Environ.* 280 (2021), 119418.
- [54] M.S. Elovitz, U. von Gunten, Hydroxyl radical/ozone ratios during ozonation processes. I. The R_{ct} concept, *Ozone. Sci. Eng.* 21 (1999) 239–260.
- [55] S. Afzal, X. Qian, J. Zhang, High surface area mesoporous nanocast LaMO_3 ($\text{M}=\text{Mn}, \text{Fe}$) perovskites for efficient catalytic ozonation and an insight into probable catalytic mechanism, *Appl. Catal. B Environ.* 206 (2017) 692–703.
- [56] L. Yang, C. Hu, Y. Nie, J. Qu, Catalytic ozonation of selected pharmaceuticals over mesoporous alumina-supported manganese oxide, *Environ. Sci. Technol.* 43 (2009) 2525–2529.
- [57] Y. Wang, L. Chen, H. Cao, Z. Chi, C. Chen, X. Duan, Y. Xie, F. Qi, W. Song, J. Liu, S. Wang, Role of oxygen vacancies and Mn sites in hierarchical $\text{Mn}_2\text{O}_3/\text{LaMnO}_3$ - δ perovskite composites for aqueous organic pollutants decontamination, *Appl. Catal. B Environ.* 245 (2019) 546–554.
- [58] D. Wang, H. Xu, J. Ma, S. Giannakis, X. Lu, H. Chi, S. Song, J. Qi, Enhanced mineralization of atrazine by surface induced hydroxyl radicals over light-weight granular mixed-quartz sands with ozone, *Water Res.* 149 (2019) 136–148.
- [59] C.A. Emeis, Determination of integrated molar extinction coefficients for infrared absorption bands of pyridine adsorbed on solid acid catalysts, *J. Catal.* 141 (1993) 347–354.
- [60] C. Cai, X. Duan, X. Xie, S. Kang, C. Liao, J. Dong, Y. Liu, S. Xiang, D.D. Dionysiou, Efficient degradation of clofibric acid by heterogeneous catalytic ozonation using CoFe_2O_4 catalyst in water, *J. Hazard. Mater.* 410 (2021), 124604.
- [61] T. Zhang, W. Li, J.P. Croue, Catalytic ozonation of oxalate with a cerium supported palladium oxide: an efficient degradation not relying on hydroxyl radical oxidation, *Environ. Sci. Technol.* 45 (2011) 9339–9346.

- [62] H. Zhao, Y. Dong, P. Jiang, G. Wang, J. Zhang, K. Li, An insight into the kinetics and interface sensitivity for catalytic ozonation: the case of nano-sized NiFe_2O_4 , *Catal. Sci. Technol.* 4 (2014) 494–501.
- [63] T. Watanabe, N. Teshima, S. Nakano, T. Kawashima, Flow-injection/standard subtraction method for the determination of iron (III) based on its catalytic effect and inhibition of EDTA, *Anal. Chim. Acta* 374 (1998) 303–307.
- [64] G. Zhu, J. Zhu, W. Jiang, Z. Zhang, J. Wang, Y. Zhu, Q. Zhang, Surface oxygen vacancy induced $\alpha\text{-MnO}_2$ nanofiber for highly efficient ozone elimination, *Appl. Catal. B Environ.* 209 (2017) 729–737.
- [65] Z.-B. Sun, Y.-N. Si, S.-N. Zhao, Q.-Y. Wang, S.-Q. Zang, Ozone decomposition by a manganese-organic framework over the entire humidity range, *J. Am. Chem. Soc.* 143 (2021) 5150–5157.
- [66] W. Li, G.V. Gibbs, S.T. Oyama, Mechanism of ozone decomposition on a manganese oxide catalyst. 1. In situ Raman spectroscopy and ab initio molecular orbital calculations, *J. Am. Chem. Soc.* 120 (1998) 9041–9046.
- [67] K.M. Bulanin, J.C. Lavalley, J. Lamotte, L. Marley, N.M. Tsyganenko, A. A. Tsyganenko, Infrared study of ozone adsorption on CeO_2 , *J. Phys. Chem. B* 102 (1998) 6809–6816.
- [68] S. Afzal, X. Quan, S. Lu, Catalytic performance and an insight into the mechanism of CeO_2 nanocrystals with different exposed facets in catalytic ozonation of p-nitrophenol, *Appl. Catal. B Environ.* 248 (2019) 526–537.
- [69] C. Tang, C. Chen, H. Zhang, J. Zhang, Z. Li, Enhancement of degradation for nitrogen doped zinc oxide to degrade methylene blue, *Phys. B Condens. Matter* 583 (2020), 412029.
- [70] Q. Zhang, C.S. Dandeneau, X. Zhou, G. Cao, ZnO nanostructures for dye-sensitized solar cells, *Adv. Mater.* 21 (2009) 4087–4108.